Biometals (2012) 25:393–412
DOI 10.1007/s10534-011-9513-7

Trace metal complexation by the triscatecholate siderophore protochelin: structure and stability

James M. Harrington · John R. Bargar · Andrzej A. Jarzecki · James G. Roberts · Leslie A. Sombers · Owen W. Duckworth

Received: 11 November 2011 / Accepted: 1 December 2011 / Published online: 21 December 2011

Abstract Although siderophores are generally viewed as biological iron uptake agents, recent evidence has shown that they may play significant roles in the biogeochemical cycling and biological uptake of other metals. One such siderophore that is produced by *A. vinelandii* is the triscatecholate protochelin. In this study, we probe the solution chemistry of protochelin and its complexes with environmentally relevant trace metals to better understand its effect on metal uptake and cycling. Protochelin exhibits low solubility below pH 7.5 and degrades gradually in solution. Electrochemical measurements of protochelin and metal–protochelin complexes reveal a ligand half-wave potential of 200 mV. The Fe(III)Proto^{3-} complex exhibits a salicylate shift in coordination mode at circumneutral to acidic pH. Coordination of Mn(II) by protochelin above pH 8.0 promotes gradual air oxidation of the metal center to Mn(III), which accelerates at higher pH values. The Mn(III)Proto^{3-} complex was found to have a stability constant of log $\beta_{110} = 41.6$. Structural parameters derived from spectroscopic measurements and quantum mechanical calculations provide insights into the stability of the Fe(III)Proto^{3-}, Fe(III)H_3Proto, and Mn(III)-Proto^{3-} complexes. Complexation of Co(II) by protochelin results in redox cycling of Co, accompanied by accelerated degradation of the ligand at all solution pH values. These results are discussed in terms of the role of catecholate siderophores in environmental trace metal cycling and intracellular metal release.

Keywords Siderophores · Catechol · Iron · Manganese · Cobalt · Complexation

Electronic supplementary material The online version of this article (doi:10.1007/s10534-011-9513-7) contains supplementary material, which is available to authorized users.

J. M. Harrington · O. W. Duckworth (✉)
Soil Science Department, North Carolina State University, Raleigh, NC 27695-7619, USA
e-mail: owen_duckworth@ncsu.edu

Present Address:
J. M. Harrington
U.S. Environmental Protection Agency, National Exposure Research Laboratory, Research Triangle Park, NC 27711, USA

J. R. Bargar
Stanford Synchrotron Radiation Lightsource, 2575 Sand Hill Rd., Bldg. 137, MS 69, Menlo Park, CA 94025, USA

A. A. Jarzecki
Chemistry Department, The Brooklyn College and the Graduate School of the City University of New York, Brooklyn, NY 11210, USA

J. G. Roberts · L. A. Sombers
Chemistry Department, North Carolina State University, Raleigh, NC 27695-8204, USA

Introduction

Specific trace metals are essential to the metabolic activity of all organisms, and scarcity of metals may be

an important factor in limiting organism growth. One strategy that plants and microbes use to obtain these trace metals is the production and exudation of biomolecules that solubilize metals, return them to the cell, and facilitate their uptake for use by the organism (Crumbliss and Harrington 2009; Raymond and Dertz 2004; Renshaw et al. 2002; Kraemer et al. 2005; Marschner et al. 1986). Siderophores, a class of biogenic ligands that are traditionally associated with the mobilization and uptake of Fe(III), have a high degree of structural variability in terms of their binding groups and backbone structure (Hider and Kong 2010). Despite this structural diversity, these molecules broadly make use of large binding affinities and relatively slow exchange kinetics to bind and solubilize metals.

One feature that contributes to the structural variability of siderophores and plays a significant role in determining the reactivity of siderophores is the identity of the donor groups that bind the metal ion. The majority of siderophores achieve selective complexation of hard metal ions, as well as stabilization of higher oxidation states, through coordination by hard donor atoms (viz. charged oxygen in specific moieties, such as catechol moieties), which are contained in numerous bacterial siderophores such as enterobactin, petrobactin, and azotochelin (Fig. 1). Catechol donor groups bind Fe(III) through the conjugated central ring system, which delocalizes electron density (Albrecht-Gary and Crumbliss 1998). Catecholate siderophores are produced by many soil and pathogenic bacteria and may also be produced by marine organisms (Clarke et al. 2001; Winkelmann 2004; Kraemer et al. 2005).

An environmentally important catecholate siderophore is protochelin (Fig. 1), which is produced by the free-living diazotroph *Azotobacter vinelandii* (Cornish and Page 1995). Catecholate siderophores are one of the few ligands that bind molybdate at circumneutral pH, although these complexes have significantly lower stability constants than those of the ligand with Fe(III) (Duhme et al. 1998; Bellenger et al. 2007; Khodr et al. 2002; Cornish and Page 2000). Protochelin has been implicated in the specific transport of Mo and V (in addition to Fe) in *A. vinelandii* (Bellenger et al. 2008a, b), which uses these metals in nitrogenase enzymes (Bellenger et al. 2011). Protochelin is also associated with the specific rejection of toxic W (Wichard et al. 2008), and the ability to form complexes with many metals coupled with selectivity of the uptake may function as a detoxification mechanism to exclude toxic metals (Kraepiel et al. 2009). Coupled with a growing body of work that has explored the geochemistry and biology of non-ferric metal interactions with other siderophores (Duckworth et al. 2008b; Duckworth and Sposito 2005; Parker et al. 2004, 2007; Boukhalfa et al. 2004, 2007; Neu et al. 2005; Harris et al. 2007; Mishra et al. 2009; Dahlheimer et al. 2007; Frazier et al. 2005; Szabo and Farkas 2011), work with protochelin has led to the suggestion that siderophores may be involved with the

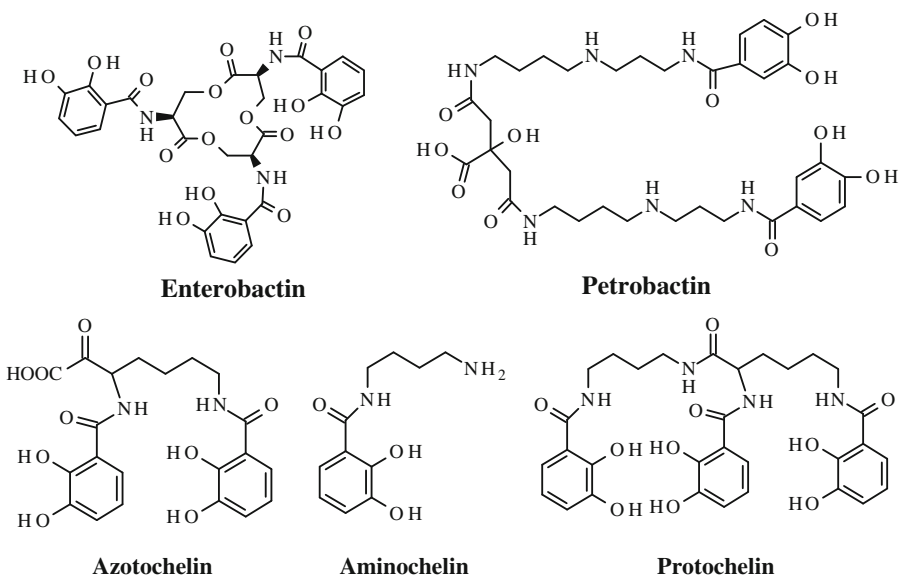

Fig. 1 Structures of the catecholate siderophores enterobactin, petrobactin, azotochelin, aminochelin, and protochelin

transport of non-ferric metals (Kraepiel et al. 2009) and have a diverse chemistry with a variety of environmentally relevant metals (Duckworth et al. 2009a).

Despite the proposed role that siderophores play in the cycling of non-ferric metals in the environment and the observed interactions of Mo and V with protochelin, very little work has been done to characterize the binding reactions of common non-ferric metals with catecholate siderophores. In this study, we investigated the fundamental solution properties of the bacterial siderophore, protochelin, and the binding characteristics of Fe(III) protochelin complexes. Additionally, we explored the structure and stability of its complexes with common first-row transition metals that may form strong complexes with siderophores (viz. Mn, Co, and Cr) by using spectroscopic and computational methods (Duckworth et al. 2009a; Hernlem et al. 1999). The results will then be discussed in terms of the role of protochelin and catecholate siderophores in the environmental cycling of metals and the cellular uptake of metals.

Materials and methods

Materials

All solutions were prepared in ASTM Type I deionized water (resistivity = 18 MΩ cm). Protochelin was prepared synthetically by the Small Molecule Synthesis Facility (SMSF) at Duke University using a previously reported procedure (Duhme et al. 1997), and was used as received. The purity of the sample was verified by nuclear magnetic resonance spectroscopy and liquid chromatography-mass spectrometry at the SMSF (data not shown). Desferrioxamine B mesylate (DFOB; 95%) was purchased from Sigma-Aldrich and used as obtained. The preparation of metal–protochelin complexes was performed as described in the Supporting Information. Buffers used will be noted where appropriate. For electrochemical studies, all chemicals were purchased from Sigma-Aldrich (St. Louis, MO) and used as received, unless otherwise noted.

Solution pH was measured with an Accumet XL20 pH meter (Fisher Scientific) equipped with a 410 Micro-combination pH probe (Microelectrodes, Inc). Solution pH was controlled through addition of measured volumes of standardized 0.10 M HCl and 0.10 M NaOH, purchased from Sigma-Aldrich, unless otherwise noted. Electrodes were standardized by using commercial buffers (Fisher) at pH 4.0, 7.0, and 10.0. UV–visible spectra were measured using an Ocean Optics Jaz spectrophotometer equipped with an external dip probe for pH-dependent spectrophotometric titrations and a fiber-optic 1 cm path length cell for competition titrations.

Ligand characterization

Ligand solubility was characterized by preparing two solutions of protochelin dissolved in buffer solutions. The first solution was prepared by massing 50.0 mg of solid protochelin and adding 50 ml of a buffer solution of 0.10 M HEPES in 0.10 M NaCl at pH 7.0. The second solution was prepared by massing 50.0 mg of solid protochelin and adding 50 ml of a buffer solution of 0.10 M MOPS in 0.10 M NaCl at pH 8.0. Both solutions were sonicated for 15 min, and the solution was filtered through a 0.22 μm filter into a cuvet to remove any undissolved particulate matter. The UV–visible absorbance of the solution was measured and the molar absorbance at the measured $\lambda_{max} = 316$ nm was used to determine the concentration of the ligand in solution.

Ligand stability was characterized by spectrophotometric kinetic measurement of the degradation reaction. Solutions were prepared by adding the ligand to aqueous solutions of 0.10 M NaCl at a pH below that is required to dissolve the ligand. To these solutions, a measured volume of buffer in 0.10 M NaCl was added to adjust the solution pH, followed by rapid dilution to the final volume and measurement of the initial spectrum. Subsequent spectra were measured regularly to monitor the degree of ligand degradation. Reaction temperature was controlled at 25°C with a temperature-controlled water bath. The concentration of buffer used in all experiments was 0.010 M. At pH 8.0, the buffer used was MOPS, whereas all other experiments at pH 8.5, 9.0, 9.5, and 10.0 contained CHES.

Fe(III)–protochelin spectrophotometric titration

To characterize the binding mode of the Fe(III) with protochelin, a pH-dependent UV–visible spectrophotometric titration was performed. A solution of

4.1×10^{-5} M Fe(III) and protochelin was prepared at pH = 9.1 as described in Supplemental Material. The Fe(III) and protochelin solution was titrated with measured volumes of 0.10 M HCl with stirring. At each addition, the final pH was recorded and the UV–visible spectrum over the range of 250–800 nm was measured. The reaction temperature was controlled at 25°C using a temperature-controlled water bath.

Mass spectrometry analysis of the degradation products of protochelin and the metal–protochelin complexes

Mass spectrometry of samples was performed using Electrospray Ionization (ESI) on an Agilent Technologies (Santa Clara, CA) 6210 LC-TOF mass spectrometer. Solutions of protochelin and of the Mn–Proto and Co–Proto complexes were prepared at a concentration of 1.0 mM as described above and in the Supplemental Material. Samples were diluted in methanol and analyzed via a 1 µl flow injection at 300 µl/min in a water:methanol mixture (25:75 v/v) with 0.1% ammonium hydroxide. The mass spectrometer was operated in negative-ion mode with a capillary voltage of 3.5 kV, nebulizer pressure of 50 psig, and a drying gas flow rate of 10 l/min at 350°C. The fragmentor and skimmer voltages were 110 and 65 V respectively. Reference ions of purine at *m/z* 112.9855 and HP-0921 at *m/z* 966.0007 were simultaneously introduced via a second orthogonal sprayer, and used as internal calibrants. Mass spectra of the protochelin solution, the Mn–Proto solution, and the Co–Proto solution are shown in the Supplemental Material.

Computations of metal–protochelin complexes

All structure and frequency calculations reported here were carried out by the Gaussian 09 program package (Frisch et al. 2009). Molecular structures were found by full geometry optimization at the B3LYP/6-31G* exchange–correlation hybrid of density functional (Becke 1993; Lee et al. 1988). Computed frequencies of all structures are positive, indicating that the optimized structures are at real minima of their ground-state potential energy surfaces. To simulate complexes in aqueous solutions, density functional theory (DFT) calculations were embedded in the polarizable cavity with a static dielectric constant ($\varepsilon = 78.355$) and by making the solvent reaction field self-consistent with the solute electrostatic potential, commonly referred to as the Polarizable Continuum Model (PCM) implemented in Gaussian 09 (Tomasi et al. 2005).

X-ray spectroscopy of metal–protochelin complexes

K-edge X-ray fluorescence-yield (FY) spectra of the metal centers in solutions containing Fe(III) and protochelin (5 mM; pH = 7.5 and 10 mM; pH = 4) were measured at Stanford Synchrotron Radiation Lightsource (SSRL) Beamline 11-2 [Si (220) variable-exit monochromator] at room temperature using a 30-element Ge fluorescence detector. Mn(III)Proto^{3-} (5 mM; pH = 9.3) and Co–Proto (5 mM; pH = 8.0) FY spectra were measured in a liquid helium cryostat (7–13°K) using a 30-element Ge fluorescence detector to retard the rate of photolytic degradation of these complexes. Frozen samples contained 40% glycerol to reduce formation of ice crystals (Levina et al. 2005). Cr–Proto (5 mM; pH = 8) FY spectra were measured at SSRL Beamline 4-3 [Si (111) variable-exit monochromator] using a Lytle-type ionization-chamber detector. Harmonics were rejected using Rh-coated mirrors and/or by detuning the monochromators. In all cases, spectra were collected using Soller slits and Z-1 X-ray filters to reduce the intensity elastic scattering received by the detectors. For the Fe-, Co-, and Cr-siderophore complexes, energy calibration was maintained using metal foils; for the Mn–siderophore complex, calibration was accomplished by adjusting the E_0 of potassium permanganate ($KMnO_4$). In the measurements of the Fe(III)-Proto samples, at least five spectra were averaged for each sample to improve signal-to-noise ratio. The Mn(III)Proto^{3-} complex exhibited slight beam damage after the initial scan (shown in Fig. S1) and thus only one scan was used. Spectra were dead-time corrected, energy calibrated, averaged, background-subtracted, splined, and fit in *R*-space (Kelly et al. 2008) using the SixPACK interface (Webb 2005), which makes use of the IFEFFIT code (Newville 2001).

The relative fraction of Mn(II) in the initial and successive scans of the Mn(III)Proto^{3-} sample (i.e., due to photolytic beam reduction) was assessed by (a) comparing the first Mn(III)Proto^{3-} scan to spectra from the more Mn(II)HDFOB^{0} and Mn(III)HDFOB^{+} complexes (by linear combination fitting over the energy range 6,400–6,800 eV) (Duckworth et al. 2009c), and (b) by

fitting the successive Mn(III)Proto^{3-} scans as a linear combination of X-ray Absorption Near-Edge Structure (XANES) from Mn(II)Cl_2 and Mn(III)Proto^{3-} (first scan).

Amplitude and phase functions were calculated using FEFF 9 [Dirac-Hara exchange potentials (Rehr et al. 2009)], and structural models for Mn(III)-Proto^{3-}, Fe(III)Proto^{3-}, and Fe(III)H_3Proto complexes were obtained from DFT calculations. EXAFS data were fit using a common value of the parameter ΔE_0, which was allowed to float during optimization. The amplitude reduction factor (S_0^2) was fixed at 0.87 for Fe and 0.835 for Mn based on prior work (Duckworth et al. 2008a; Webb et al. 2005b). The Debye–Waller disorder parameter (σ^2) and the interatomic distance (R) for each shell were floated freely during optimization. Development of the structural models used to fit spectra is described in detail in the Supplemental Material.

Competition of Fe(III) and Mn(III) for protochelin and desferrioxamine B

For determination of the Mn(III)Proto^{3-} stability constant, a competition experiment was performed between the Fe(III)Proto^{3-} complex and the Mn(III)HDFOB^{+} complex. A solution of 0.4 mM Fe(III)Proto^{3-} was prepared as described in the Supplemental Material. A second solution of 2.0 mM Mn(III)HDFOB^{+} was prepared using previously established air-oxidation procedures and was used in experiments (Duckworth and Sposito 2005). Solution pH was controlled with a final concentration of 0.050 M HEPES at pH = 9.05. The Fe(III)Proto^{3-} solution was separated into 5.0 ml aliquots, and varying volumes of the Mn(III)HDFOB^{+} solution were added to produce a concentration range from 0 equivalents of Mn(III) to 25 equivalents of Mn(III). After allowing 5 days equilibration time, the solution spectra and pH were measured. The spectra were measured a second time a day later to ensure that no change was taking place in the solution speciation. No appreciable shift in solution pH was measured over the course of the experiment. The computer program HYPERQUAD was used to determine the relative concentrations of each species in solution and the equilibrium constant of the Mn(III)Proto^{3-} complex from each addition (Gans et al. 1996). HYPERQUAD used an input of the spectra of all species in solution to determine the relative concentrations of the four species involved in the equilibrium. Using the determined concentrations of the species, the program is able to calculate the equilibrium constant (K_{obs}) of the following reaction:

$$\text{Mn(III)HDFOB}^{+} + \text{Fe(III)Proto}^{3-} \rightleftarrows \text{Fe(III)HDFOB}^{+} + \text{Mn(III)Proto}^{3-}\ K_{obs} \quad (1)$$

The program then uses the known log β_{110} of Fe(III)Proto^{3-}, the known stability constant of Mn(III)HDFOB^{+} and the known stability constant of Fe(III)HDFOB^{+} to determine the stability constant of Mn(III)Proto^{3-} (Eq. 2), using Eq. 3.

$$\text{Mn}^{3+} + \text{Proto}^{6-} \rightleftarrows \text{Mn(III)Proto}^{3-}\ \beta_{110,\text{Mn(III)Proto}} \quad (2)$$

$$\beta_{110,\text{Mn(III)Proto}} = \frac{K_{obs}\beta_{110,\text{Fe(III)Proto}}\beta_{110,\text{Mn(III)HDFOB}}}{\beta_{110,\text{Fe(III)HDFOB}}} \quad (3)$$

Analysis of the UV–visible spectra was performed in 1.0 nm increments over the wavelength range of 310–750 nm. For the determination of the Mn(III)-Proto^{3-} formation constant, protonation constants of protochelin and Fe(III) complex stability constants were taken from the literature (Duhme et al. 1997). Protonation constants, Fe(III) complex formation constants, and Mn(III) complex formation constants for DFOB were also taken from the literature (Duckworth and Sposito 2005; Schwarzenbach and Schwarzenbach 1963). For solution of equilibrium concentrations, reference spectra were loaded for Mn(III)Proto^{3-}, Fe(III)Proto^{3-}, Mn(III)HDFOB^{+}, and Fe(III)HDFOB^{+}.

Background-subtracted fast-scan cyclic voltammetry (FSCV)

A physiologically buffered solution (phosphate buffered saline) at pH = 7.4 was used in all flow injection analysis experiments. All aqueous solutions were prepared using doubly deionized water (Barnstead EasyPure II, Dubuque, IA).

Carbon-fiber microelectrodes were fabricated as described previously (Sanford et al. 2010). Briefly, a single 7 μm diameter T-650 carbon fiber (Cytec Industries, West Patterson NJ) was aspirated into a single borosilicate glass capillary (A-M Systems, Sequim, WA) and tapered using a micropipette puller

(Narishige, Tokyo, Japan) to form two sealed microelectrodes. The exposed length of carbon fiber was cut to approximately 100 μm, and an electrical connection was made by backfilling the capillary with an ionic solution and inserting a lead. A Ag/AgCl pellet reference electrode (World Precision Instruments, Sarasota, FL) was employed to complete the two electrode electrochemical cell.

A syringe pump (New Era Pump Systems, Wantagh, NY) supplied a continuous buffer flow of 1 ml/min across the working and reference electrodes. The working electrode was positioned in a custom electrochemical cell using a micromanipulator (World Precision Instruments, Sarasota, FL). Two second bolus injections of analyte to the microelectrode surface were accomplished with a six-port HPLC valve mounted on a two-position air actuator controlled by a digital pneumatic solenoid valve (Valco Instruments, Houston TX). The entire apparatus was housed within a custom-built grounded Faraday cage. In most experiments, an inverted triangular waveform ranging from +0.8 to −0.8 V with a holding potential of +0.8 V versus Ag/AgCl was applied at a scan rate of 100 V/s, and at a frequency of 10 Hz using a custom built instrument for potential application to the electrochemical cell and for current transduction (University of North Carolina at Chapel Hill, Department of Chemistry, Electronics Facility). Complete cyclic voltammograms of protochelin were collected in ~50 ms. All experiments were performed at room temperature. TH-1 software (ESA, Chelmsford, MA) was used for waveform output and data collection with a DAC/ADC card (6251, National Instruments, Austin, TX). A second card (6711) was used for triggering the DACs and ADCs and for synchronization of the electrochemical experiment with the flow injection system. Signal processing including background subtraction, signal averaging, and digital filtering (low-pass filtered at 2 kHz) was software-controlled. Statistical and graphical analysis was accomplished using GraphPad Prism 5 (GraphPad Software, Inc., La Jolla, CA).

Results and discussion

Solubility of protochelin

Previous reports on the ligand protochelin have generally focused on the production of the ligand and its Fe or Mo binding properties (Cornish and Page 1995, 2000; Duhme et al. 1997; Taraz et al. 1990; Bellenger et al. 2008b). In these reports, there is very little mention of the solution properties of free protochelin. To addresses this basic knowledge gap, we conducted a characterization of the solubility and stability of protochelin. A semi-quantitative determination of protochelin found that its solubility at pH = 7.0 is approximately 2.4×10^{-4} M; at pH = 8.0, the solubility of the molecule is significantly higher (>1.0 mM). It is impractical to determine the exact solubility of the ligand at this pH due to the large masses of ligand required for such an experiment. Between pH of 7.0 and 8.0, the ligand undergoes a spectral shift consistent with protonation of the catechol donor groups, making characterization of the solubility in this range difficult. The low solubility of the protonated form (neutral) of protochelin can easily be rationalized from a simple analysis of the structure of the molecule (Fig. 1). The backbone of the molecule features very few hydrogen bond donor or acceptor sites, and the catechol donor groups of the molecule are likely protonated at pH < 7.5 (Loomis and Raymond 1991), resulting in a neutral charge and highly hydrophobic donor groups at low solution pH (Harris et al. 1979b). The limited solubility of protochelin at circumneutral to acidic pH may affect laboratory experiments; however, it is unlikely to constrain protochelin mobility and efficacy in an environmental setting, where ligand concentrations are significantly lower than those utilized in the studies presented here (Winkelmann 2007; Essén et al. 2006). Although concentrations of protochelin in soils and natural waters have not been measured, environmental concentrations of individual siderophore are typically on the order of picomolar to 10s of nanomolar (Holmström et al. 2004; Duckworth et al. 2009b; Mucha et al. 1999; Mawji et al. 2008) as compared to the millimolar concentrations used here.

Degradation of protochelin and metal–protochelin complexes

Soluble protochelin degrades slowly over time. At the low end of the experimental pH range (<7.5), the ligand was found to be stable in solution over extended periods of time, as long as 5 days in solution. However, as the solution pH increased, the ligand was found to be unstable, as evidenced by the gradual

increase in solution turbidity and changes in the UV–visible absorbance spectra (Fig. 2). Attempts to quantify the rate of degradation as a function of pH (not shown) exhibited a high degree of variability, preventing a detailed analysis of the pH-dependent reaction mechanism.

The degradation of the ligand over time was confirmed by reduction of the parent peak in mass spectra of aged solutions (cf. Supplemental Material, Figs. S2 and S3). In addition to the M^- peak (623.23 *m/z* ratio), peaks are observed at lower *m/z* ratios, suggesting degradation of the ligand. Mass spectral analysis of solutions of the Mn–Proto complex and of the Co–Proto complex (see Supplemental Material, Figs. S4–S7) exhibits a number of peaks at lower *m/z* ratios than the M^- peak at 623.23 *m/z* ratio, suggesting that the ligand degrades both in the presence and in the absence of metals. Further, after reaction times greater than 2 h, a peak is gradually observed at 982.99 *m/z* ratio in all samples and at 1,282.97 in the presence of Co(II), suggesting the possibility of phenol coupling of the ligands (Selig et al. 2003). Attempts to assign the mass spectral signals observed in the degradation experiments were unsuccessful, including assignment with the predicted hydrolytic products, azotochelin and aminochelin. It is interesting to note additionally that at longer reaction times, the mass spectral signal corresponding to the M^- peak of protochelin disappears in the presence of Co, further supporting the idea of metal-catalyzed ligand degradation. Finally, it should be noted that although mass spectral signals that appeared in the solutions of protochelin alone (146 *m/z* peak, 197 *m/z* peak) were also observed in the mass spectra measured for the M-Proto^{3-} systems, a number of novel low *m/z* peaks were observed in the presence of the metals.

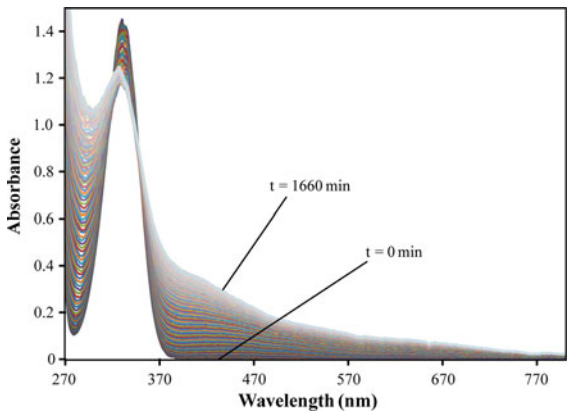

Fig. 2 *Plot* of the change in absorbance spectrum of a solution of protochelin over time as ligand degradation occurs. Conditions: [Ligand] = 6.4×10^{-5} M, pH = 9.5, $\mu = 0.10$ M (NaCl), 0.10 M CHES, $T = 25°C$

Collectively, these observations suggest that the ligand decomposes by a number of pathways. Such degradation pathways could potentially include hydrolysis and oxidation, and result in the formation of benzoquinone groups, coupled hydroxylated aromatic compounds, or a number of other organic molecules (Devlin and Harris 1984). Because some masses representing degradation products that are observed in the presence of metals are not observed in the absence of metals, metals may promote the formation of novel degradation products. Mass spectral peaks corresponding to expected hydrolysis products of the ligand were not observed, further suggesting that redox reactions may be involved in the presence of Mn and Co. In previous studies, redox degradation reactions have been shown to be more likely to occur in the presence of oxidizing agents (Schweigert et al. 2001). This process may explain degradation of the complexes studied herein over extended periods of time in the presence of Mn, and rapidly in the presence of Co, both of which are oxidizing agents in the 3+ oxidation state.

Formation of metal–protochelin complexes

In the case of stable 3+ metal ions, such as Fe, direct complex formation is possible by simple adjustment of the pH (see Supplemental Material). However, in the case of metal ions that obtain the 3+ oxidation state through redox reactions, a less direct route of complex formation must be taken. Manganese(II) oxidation in the environment, even under oxic conditions, is typically slow unless the process is mediated by bacteria or fungi (Tebo et al. 2005). However, complexation of a metal by hard donor groups such as the catechol donors of protochelin may increase the rate of oxidation and stabilize the oxidation product (Buerge and Hug 1998; Strathmann and Stone 2002). This type of reaction has been observed for Mn(III) complexes with other siderophores, namely DFOB, coprogen, and pyoverdin GB-1 (Duckworth and Sposito 2005; Parker et al. 2007; Szabo and Farkas 2011). Although the oxidation rate of Mn(II) in the presence of protochelin was not quantified, at pH = 8.5 the complex concentration reaches a

steady-state, as indicated by stability in the UV–visible spectrum after 2 h.

Like manganese, Co(II) air-oxidation does not typically occur under environmental conditions, but can be promoted by the presence of strong complexing agents (viz. ethylene diamine). In the case of the Co(III)–Proto complex, mixture of Co(II) in solution with the ligand, followed by an increase in the solution pH results in a change in the solution color that suggests that air oxidation of the metal is taking place. However, the solution gradually shifts from a green color that likely corresponds to a Co(III)–siderophore complex (Duckworth et al. 2009c) to a dark brown solution with a turbid appearance. Additionally, X-ray spectroscopy of a sample analyzed approximately 30 min after synthesis revealed a XANES white line position consistent with the presence of Co(II), and no evidence in the EXAFS spectrum of any second shell structure in the FT magnitude plot (not shown). This observation suggests that oxidation of Co(II) resulted in an unstable Co(III) complex that degraded by internal electron transfer, resulting in reaction with the catechol donor groups (Schweigert et al. 2001; Devlin and Harris 1984). A similar behavior was observed in experiments performed with the Mn–enterobactin complex, where Mn(II) oxidation over the course of 2 h at pH = 9 in the presence of enterobactin resulted in a cloudy black solution containing Mn(II) (Parker 2010, personal communication). Previous work with Co(III)HDFOB^{+} noted that, despite a high stability constant, a fraction of the complex in solution degrades to Co(II) at all pH values investigated (Duckworth et al. 2009c). In addition, Carrano et al. (1996) noted that rhizoferrin, an α-hydroxycarboxylate siderophore, does not form a stable complex with Co(III).

Attempts were made to synthesize the Cr(III)-Proto^{3-} complexes for structural analysis. However, it is difficult to synthesis these complexes by methods used for Mn or Fe because of slow rate of ligand exchange for Cr(III) (Hewkin and Prince 1970). The FT magnitude of EXAFS spectrum for Cr–Proto synthesized by exchange reaction (data not shown) exhibited no second shell structure, suggesting that no complex had formed.

Determination of Mn(III)Proto^{3-} stability constant

The absorbance spectra measured during the exchange reaction of Fe(III)Proto^{3-} with Mn(III)HDFOB^{+} are shown in Fig. 3. The initial spectrum (labeled 0:1 in Fig. 3) exhibits a spectral handle consistent with formation of triscatecholate-coordinated Fe(III) (λ_{max} = 492 nm), suggesting that Fe(III) is completely coordinated by protochelin. Addition of Mn(III)HDFOB^{+} results in an increase in absorbance in the UV region, a result of a large excess of unreacted Mn(III)HDFOB^{+} in solution (λ_{max} = 310 nm). The isosbestic point evident at 490 nm indicates conversion of the Fe(III)Proto^{3-} complex to the Fe(III)HDFOB^{+} complex as the concentration of added Mn(III)HDFOB^{+} increases. The maximum degree of exchange observed during these experiments was 90% exchange. As determined by fitting in HYPERQUAD, the stability constant from three replicate titrations was found to be log $\beta_{110} = 41.6 \pm 0.3$.

The Mn(III)Proto^{3-} stability constant can be compared to Mn(III)HDFOB^{+} and Fe(III)Proto^{3-} (Table 1). The Mn(III)Proto^{3-} complex is higher than that of the Mn(III)HDFOB^{+}, which is consistent with trends for Fe(III) complexes. Fe(III) exhibits high stability with protochelin due to electron resonance in the conjugated ring system of the catechol donor groups (Albrecht-Gary and Crumbliss 1998), and this phenomenon may also be responsible for the high stability of Mn(III)Proto^{3-}. However, the value determined here for the metal stability constant of Mn(III)Proto^{3-} is somewhat lower than that of Fe(III)Proto^{3-}, with a three order of magnitude difference in stability (Duhme et al.

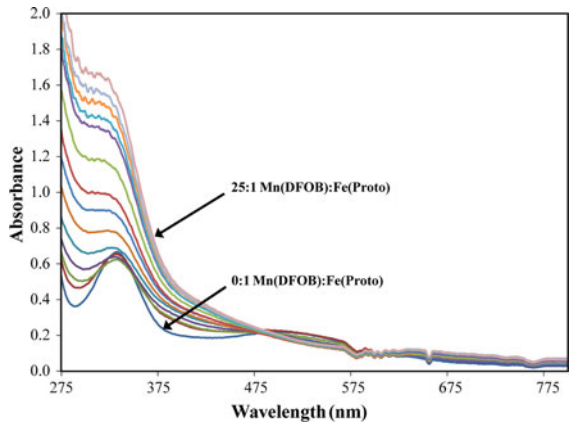

Fig. 3 UV–visible spectra obtained from the competition experiment between the Fe(III)Proto^{3-} complex and the Mn(III)HDFOB^{+} complex. The concentration ratio of Mn(III)HDFOB^{+} to Fe(III)Proto^{3-} ranges from 0 equivalents Mn(III)HDFOB^{+} to 25 equivalents Mn(III)HDFOB^{+}. Experiment was performed in HEPES buffer at pH = 9.05, T = 25°C and μ = 0.10 M (NaCl)

Table 1 Log of the stability constant of the metal complexes of a number of siderophores ($T = 25°C$)

Equilibrium	Mn(III)	Fe(III)
$HDFOB^{2-} + M(III) \rightleftarrows M(III)HDFOB^{+}$	29.9[a]	32.02[b]
$Ent^{6-} + M(III) \rightleftarrows DM(III)Ent^{3-}$	N/A	49[c]
$Proto^{6-} + M(III) \rightleftarrows DM(III)Proto^{3-}$	41.6 ± 0.3[d]	44.6[e]

Structures of Ent and Proto siderophores are shown in Fig. 1

[a] $\mu = 0$ M (Duckworth and Sposito 2005)

[b] $\mu = 0$ M (Kraemer 2004)

[c] $\mu = 0.1$ M (Loomis and Raymond 1991)

[d] This work, $\mu = 0.1$ M (NaCl)

[e] $\mu = 0.1$ M (Duhme et al. 1997)

1997). The trend in stability constants observed for the protochelin system is consistent with that of DFOB, where the $Mn(III)HDFOB^{+}$ (log $\beta_{110} = 29.9$) was found to have a stability constant just over two orders of magnitude lower than that of the $Fe(III)HDFOB^{+}$ complex (log $\beta_{110} = 32.02$) (Duckworth and Sposito 2005; Martell and Smith 2003). The significant difference between the stability constants of the Mn(III) complexes of DFOB and protochelin ($\Delta\log\beta = 11.7$) is also consistent with the difference observed between the Fe(III) complexes of DFOB and protochelin ($\Delta\log\beta = 12.6$).

A similar comparison may be made between the *p*M values of protochelin with Mn(III) and Fe(III). The *p*M values are calculated values of the free metal ions in solution (excluding hydrolysis products) at set conditions, usually 1×10^{-6} M metal, 1×10^{-5} M ligand, pH = 7.4, $\mu = 0.10$ M, and $T = 25°C$ (Harris et al. 1979a). As the complex stoichiometry is the same between the two complexes, the *p*Mn value (25.40) and the *p*Fe value (28.40) of protochelin also differ by three orders of magnitude, demonstrating the relatively lower stability of the $Mn(III)Proto^{3-}$ complex compared to the $Fe(III)Proto^{3-}$ complex. Comparison of the *p*M values to the known *p*Fe of enterobactin (35.6) demonstrates the relatively lower complex stability of the protochelin complexes than that of enterobactin (Hay et al. 2001).

Fe(III)–protochelin complex coordination modes

The spectra measured during the spectrophotometric titration of Fe(III) in the presence of protochelin are shown in Fig. 4. A gradual shift was observed in the

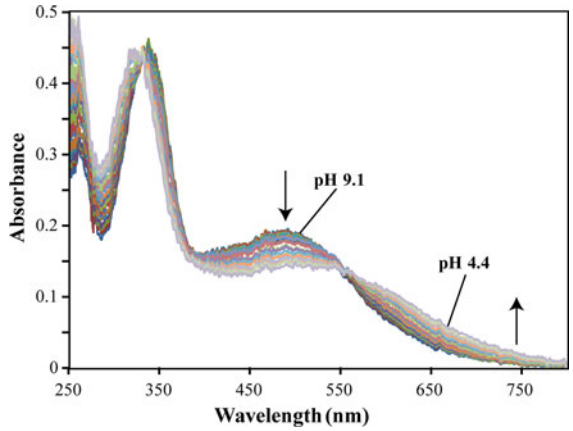

Fig. 4 Spectrophotometric titration of the $Fe(III)Proto^{3-}$ system as a function of pH from pH 9.1 to 4.4. Conditions: $[Fe^{3+}]_{tot} = 4.0 \times 10^{-5}$ M, $[Proto]_{tot} = 4.1 \times 10^{-5}$ M, $T = 25°C$, $\mu = 0.10$ (NaCl). *Arrows* indicate the direction of spectral shifts with decreasing pH

spectral maximum over the course of the titration, from 492 nm at pH = 9.1 to 545 nm at pH = 4.4. The majority of the spectral shift was observed over the pH range of 7.0–4.4. An isosbestic point was observed at 547 nm, indicating the observation of a single equilibrium over the course of the titration. The initial wavelength is consistent with the formation of the $Fe(III)Proto^{3-}$ complex (Duhme et al. 1997). An additional shift in the λ_{max} of the peak located at lower wavelengths was observed from 333 nm at pH = 7.0 to 319 nm at pH = 4.4. Below pH = 4.4, the spectrum began to decrease in intensity until a gray precipitate was observed in solution at pH = 3.8. The spectra changed negligibly through pH = 10.2 (data not shown), suggesting no change in binding mode or speciation at basic conditions.

Many siderophores feature ionizable donor groups, which play a strong role in determining the solution thermodynamics and speciation of siderophore complexes. Upon a decrease in solution pH, a high concentration of protons may compete with metals in solution for accepting electron density from the donor atoms. In donor groups such as hydroxamates or carboxylates, protonation of the donor atom generally results in dissociation of the donor group. In previous studies of catecholamide donor group siderophores, however, it has been shown that a coordination shift in the binding mode of the catecholamide donor groups will occur upon decrease in the system pH, as shown in Eq. 4 (Abergel et al. 2006).

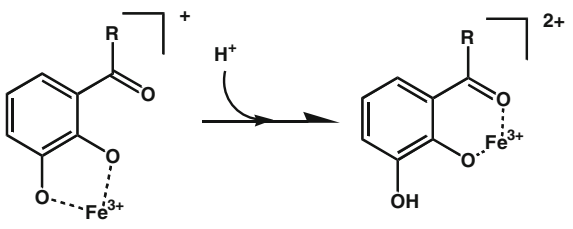

4

Protonation occurs at the distal hydroxyl donor of each catecholamide donor group, and the binding mode shifts from the catecholate mode to the salicylate mode. In a previous study, the stability of the Fe(III)Proto^{3-} complex was determined; however, the protonation of the Fe(III)Proto^{3-} complex was not characterized (Duhme et al. 1997). The spectrophotometric titration of the Fe(III)Proto^{3-} complex over the pH range of 7.0–2.8 shows a gradual shift in the observed λ_{max} of the solution from 492 nm at pH = 7.0 to λ_{max} = 547 nm at pH $\leq$ 4.4, consistent with a shift in complex binding mode from catecholate to salicylate binding mode, as seen in Eq. 4 (Hou et al. 1997; Abergel et al. 2006).

A similar experiment was performed with the Mn(III)Proto^{3-} complex, but titration to solution pH $\leq$ 6.0 resulted in little shift in solution absorbance values before the ligand precipitated out of solution. In all likelihood, a decrease in solution pH results in destabilization of the Mn(III) oxidation state, leading to reduction of Mn to the 2+ oxidation state, as has been observed for Mn(III)HDFOB^{+} at pH $<$ 7 (Duckworth and Sposito 2005). Due to the selectivity of protochelin for higher oxidation state metals, the Mn(II)Proto^{4-} and Mn(II)H$_3$Proto^{-} complexes should have markedly lower stability constants than Mn(III)-Proto complexes. This difference in stability between the two oxidation states may be compounded by the salicylate shift, possibly making complexation at lower pH even less stable than at higher pH values.

Redox chemistry of protochelin and metal protochelin complexes

A representative background-subtracted cyclic voltammogram for protochelin in the absence of a metal ion is shown in Fig. 5 (black), using a waveform ranging from −0.4 to +1.3 V at 400 V/s. This waveform is optimal for detecting dopamine, a catecholamine that is commonly studied using carbon-fiber electrodes (Heien et al. 2004; Roberts et al. 2010). Because dopamine's structure contains a catechol group, it is an appropriate model for comparison to protochelin. Dopamine exhibits a 2-electron redox reaction via the catechol/*ortho*-quinone couple with a half-wave potential of ~+200 mV versus NHE (gray). Protochelin's voltammogram exhibits similar peaks, corresponding to the redox conversion of its catechol functional groups to ortho-quinones.

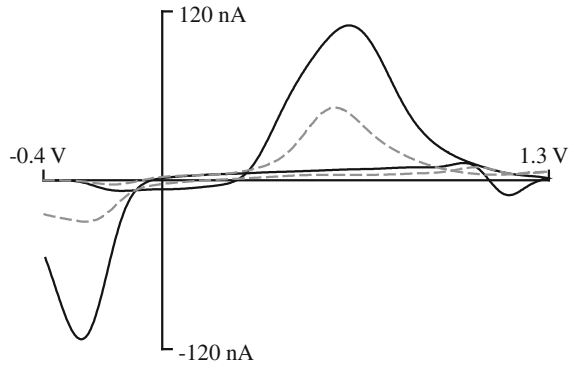

Fig. 5 Representative background-subtracted cyclic voltammograms measured for 20 μM protochelin (*black*) and 1 mM dopamine (*gray dashed*) using a waveform ranging from −0.4 to +1.3 V at 400 V/s. Dopamine is a well-studied catecholamine that exhibits a 2-electron transfer redox reaction via the catechol/*ortho*-quinone couple with a half-wave potential of ~+200 mV versus NHE. Protochelin's voltammogram exhibits similar peaks, corresponding to the redox conversion of its catechol functional groups to ortho-quinones

The redox chemistry of 10 μM protochelin was further studied using an inverted triangular waveform optimized for this molecule ranging from +0.8 to −1.2 V and scanned at 100 V/s (Fig. 6a). Addition of a metal (10 μM Mn, Fe, or Co) to protochelin reduced the overall redox current (Fig. 6b–d), consistent with a structural change upon metal coordination that inhibited the redox chemistry of the catechol groups. Distinct features associated with the complexed metal were not evident, suggesting that the catechol ligands are more redox active than the metal center. Interestingly, approximately one second into data collection, the voltammograms clearly shifted to indicate the development of a second redox process centered at a more negative potential as current resulting from the first redox reaction simultaneously decreased (Fig. 6b). In this case, adsorption of an initial layer of protochelin onto the

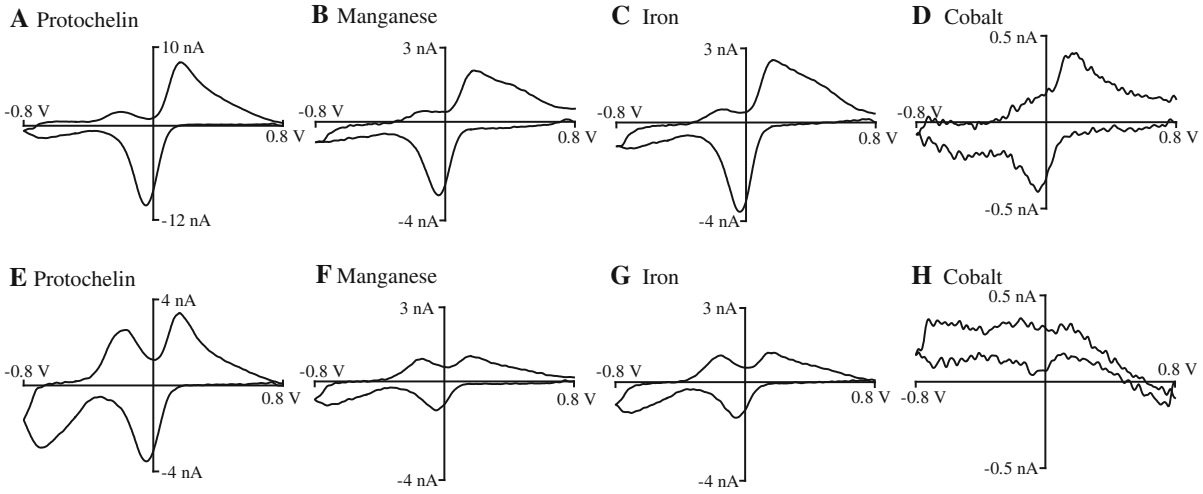

Fig. 6 Representative background-subtracted cyclic voltammograms measured for protochelin and metal–protochelin complexes of manganese(III), iron(III), and cobalt(III) (*top*, **b–d**). Interestingly, one second into data collection the voltammograms clearly shifted to indicate the presence of a second redox process developing as current resulting from the first redox reaction simultaneously decreased. Addition of a metal to protochelin reduced the overall redox current, consistent with a structural change or distortion in the catechol ligand upon binding. One second into data collection the voltammograms indicate the development of a second redox process as current resulting from the first redox reaction is simultaneously decreased (*bottom*, **e–h**)

carbon electrode may have altered the redox chemistry of protochelin molecules that were subsequently detected (see Supporting Information). Redox reactions of catechols at carbon fiber electrodes have been shown to be adsorption-controlled under similar experimental conditions (Roberts et al. 2010; Bath et al. 2000). Indeed, the current generated for the redox reaction of protochelin was found to be adsorption-controlled (rather than diffusion-controlled), by plotting cathodic peak current collected at -0.2 V as a function of scan rate ($r^2 = 0.978$, $N = 3$ electrodes, Fig. S8). A change in the solution conformation of protochelin, such as would be the result of complex formation with a metal, could suppress the ability of the molecule to adsorb onto the electrode surface, resulting in a decrease in the observed current related to the redox reaction at the catechol donor groups, as discussed above and shown in Fig. 6. In other words, upon addition of the metal, it is not likely with this type of electrode to reduce the metal center of the complex and it is less likely to oxidize the ligand (resulting in a decrease of the ligand redox signal). These results may have interesting implications regarding the possibility of metal transport by siderophores, as will be discussed later.

Metal protochelin complex computational simulations

The DFT calculations produced theoretical models of the structures of the metal–protochelin complexes in aqueous solution. These include simulations of both the catecholate and protonated salicylate form. The calculated structure of the Mn(III)Proto^{3-} complex is shown in Fig. 7. Consistent with the X-ray spectroscopic data (see below), all complexes were predicted to have a distorted octahedral configuration due to chelation through the three catechol donor groups. Selected bond lengths predicted by the computational simulation are shown in Table S1 (Supplemental Material). Within a complex, the Fe–O bond lengths of the Fe(III)Proto^{3-} complex were fairly consistent. In contrast, the Mn(III)Proto^{3-} complex was found to exhibit heavy distortion, resulting in a difference between equatorial and axial Mn–O bonds (average distance of 0.31 Å). Mn(III) has a d^4 electronic configuration, resulting in a distorted octahedral coordination sphere due to the Jahn–Teller effect. The axial bond lengths themselves are also separated by 0.18 Å, consistent with the known structure of solid phase MnOOH minerals (Kohler et al. 1997).

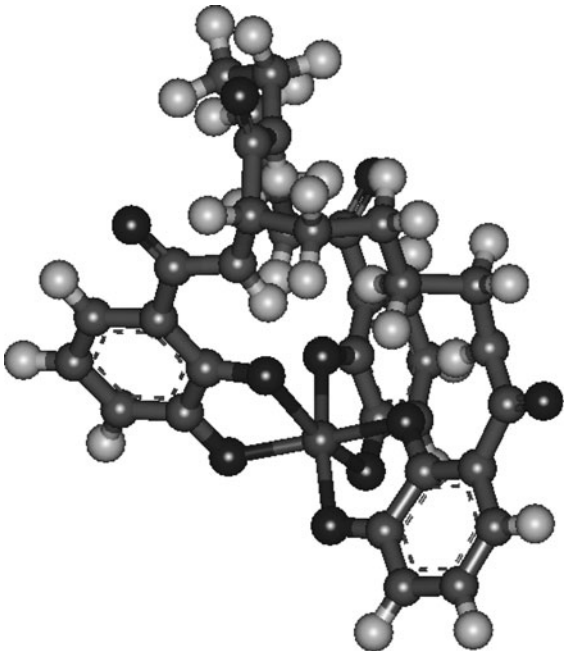

Fig. 7 Theoretical structure of the Mn(III)Proto^{3-} complex in aqueous solution calculated by DFT

The differences in the axial bond distances are reflected in bond angle distortion. There is minimal distortion of the *cis* O–M–O bond angles from their ideal values of 90° [average O–M–O bond angles of 91.4° for Mn(III)Proto^{3-}, 90.2° for Mn(III)H$_3$Proto], although the average trans angles are somewhat distorted from the ideal measurement of 180° [average O–M–O bond angles 162.4° for Mn(III)Proto^{3-} and 165.9° for Mn(III)H$_3$Proto]. This displacement of axial atoms in the same direction with an approximately planar set of four equatorial atoms results in mild distortion of average *cis*-angles and pronounced distortion of *trans*-angles. The reduced angular distortion of the theoretical Mn(III)H$_3$Proto complex [as compared to Mn(III)Proto^{3-}] is consistent with assertion that 6-membered rings may be better able to accommodate the Jahn–Teller distortion of Mn(III)-complexes (Harrington et al. 2011b).

In addition to basic structural information, energy values for the *M*(III)Proto^{3-} and *M*H$_3$Proto complexes in aqueous solution were calculated for all complexes. The calculated energies for the *M*(III)Proto^{3-} complexes and their protonated *M*(III)H$_3$Proto forms are shown in Table S2. Energy values can only be compared between systems that contain the same number of electrons and atoms. In order to obtain information regarding relative ease of protonation of metal–ligand complexes, the energy values of the complexes were set up in the form of a theoretical equilibrium, which took the form of:

$$M_1\mathrm{H_3Proto} + M_2\mathrm{Proto}^{3-} \rightleftarrows M_2\mathrm{H_3Proto} + M_1\mathrm{Proto}^{3-} \quad \log K_{ex} \tag{5}$$

where M_1 and M_2 are a first-row transition series, including Co(III), Mn(III), Cr(III), or Fe(III). To perform this comparison, the energy values (in Hartrees) on each side of the equilibrium were summed, and the difference between the two sides was taken as the difference in total strain energy of the reactants and products. The energy was converted to kJ mol^{-1}, and the resulting value was converted to an equilibrium constant (log K_{ex}) to determine which protonated complex was the more stable of the two complexes using the Gibbs free energy equation. A positive calculated log K_{ex} value signifies that the protonated product complex (M_2H$_3$Proto in Eq. 5) is favored. The resulting stability calculations demonstrate that the order of the relative ease of protonation of the four metal–protochelin complexes simulated here is Cr > Co > Mn > Fe. The energy values calculated for the *M*(III)Proto^{3-} complexes of Co(III), Cr(III), Fe(III), and Mn(III) are shown in Table S2. Although it is not possible to observe all of the metal–protochelin complexes in solution, it can be informative to use theoretical simulations of the complexes to discern information regarding their reactivity. Computational simulations, such as those obtained using DFT, provide theoretical estimations of the strain energy of complexes in solution, which can be used to predict which form of a complex may be the most stable. This approach thus can provide some insight into equilibria involving the calculated complexes. One example of a complex that can be studied using computational simulations is the protonated Mn(III)H$_3$Proto complex. Our results suggest that it is not possible to protonate the Mn(III)Proto^{3-} complex without resulting in reduction of the metal and subsequent dissociation of the complex, as discussed above; however, the protonation behavior may be significant to understanding complex breakdown.

The order described previously demonstrates that the Cr(III)Proto^{3-} complex is the easiest to protonate, followed by Co(III), Mn(III), and Fe(III). Protonation

of the complex results in a shift in the coordination mode, as discussed above, to the salicylate binding mode. Such a shift in coordination mode results in a change from five-membered chelate rings to six-membered chelate rings, as well as a compression of bond lengths in the salicylate complex. Both factors may explain the trend in protonation that is observed in the theoretical calculations. Smaller metal ions form more stable complexes when six-membered chelate rings are formed with the donors of the chelators. Thus, Cr(III) and Co(III), which are the smaller of the four metals studied here (0.615 and 0.545 Å, respectively), may have a stronger preference for protonation of the catecholamide donor groups than Mn(III) and Fe(III), which are slightly larger metal ions (both 0.645 Å) (Shannon 1976). The relative increase in theoretical stability of Mn(III) to Fe(III) in six-membered rings is also consistent with a recent report that noted that six-membered ring structures may be more stable with Mn(III) because they better accommodate Jahn–Teller distortion (Harrington et al. 2011b).

Mn(III) has a d^4 electronic configuration, which, as mentioned above, results in a distorted octahedral coordination sphere due to the Jahn–Teller effect. It can also be seen in the theoretical solution structure of the Mn(III)H_3Proto complex that one of the O–C–C–O dihedral angles is highly distorted from its ideal planar orientation, at 33°. This distorted dihedral angle may be necessary for the complex to accommodate the Jahn–Teller effect, and chelation of the metal through the catecholate binding mode will not allow the ligand the flexibility necessary to reach the lowest energy conformation. This may help to explain why a shift to the salicylate binding mode is more energetically favorable for the Mn(III) complex than the Fe(III) complex.

X-ray spectroscopy of metal–protochelin complexes

Mn K-edge XANES spectra of the Mn(III)Proto^{3-} complex are shown in Fig. S1, Supplemental Material. In successive scans, the edge region of the spectrum changed shape, indicating beam-damage of the sample, even at ca. 10°K (liquid He crysostat). As beam damage occurred, the position and intensity of the white line shifted to lower energy, consistent with partial reduction of Mn to the 2+ oxidation state. The extent of reduction that occurred between the first and second scans is >7%, as determined by linear combination fit of the second scan with the first scan and aqueous Mn(II) (see Fig. S1, Supplemental Material). Only the first scan was used for subsequent analysis. The edge position and intensity of the white line of the first scan of the complex spectrum is consistent with the 3+ oxidation state of the metal, as judged using linear combinations of Mn(III)HDFOB$^+$ and Mn(II)HDFOB^0 XANES spectra. Fits to the first Mn(III)Proto^{3-} spectrum yielded a best fit containing approximately 98.8 ± 0.03% Mn(III)HDFOB$^+$, suggesting the complex predominantly contained Mn(III).

EXAFS spectra of the Fe(III)Proto^{3-}, Fe(III)H_3Proto, and Mn(III)Proto^{3-} complexes were measured and fit to structural models to elucidate their structures in solution. The complexes discussed above were fit using single scattering (SS) paths for Me-O and Me-C (2nd and 3rd shells) (cf. Table 2). Multiple-scattering shells were also utilized, as described in the Supplemental Material and shown in Table 2. In the Fe(III)Proto^{3-} complex, the large FT peak at ca. 1.5 Å ($R + \Delta R$) corresponds to EXAFS from the first O shell and exhibits $N = 5.3$ and $R = 2.000 \pm 0.006$ Å. This ca. 2.0 Å Fe–O distant is consistent with the expected structure of the Fe(III)Proto^{3-} complex, which is believed to be hexacoordinate in solution. The Fe–O bond length is consistent with a previous study of the EXAFS spectrum of the Fe(III)–enterobactin complex in catecholate coordination, which determined the same average Fe–O bond length (Abergel et al. 2006). Based on DFT calculations, the Fe(III)Proto^{3-} shell corresponding to the 2.5 Å ($R + \Delta R$) FT peak was fit using a 6-carbon shell at $R = 2.80 \pm 0.02$ Å. This result also agrees with the model proposed for enterobactin, where the second shell was found to be composed of six carbon atoms at a distance of 2.82 Å. A third shell of six proximal ring carbon atoms at 4.32 Å was needed for our fit.

The results of structural fitting of the EXAFS spectrum of the Mn(III)Proto^{3-} complex are also shown in Fig. 8 and Table 2. For this complex, a similar model was used to fit the spectrum, although it was necessary to add a fourth shell to the fit to obtain a more accurate fit. The first shell of the fit contained four oxygen atoms located at an average distance of 1.86 ± 0.01 Å, and the second shell of the fit corresponds to the remaining two oxygen atoms, which are found an average of 2.25 ± 0.03 Å from the metal

Table 2 Amplitude reduction factors, coordination numbers, interatomic distances, and Debye–Waller factors for metal–siderophore complexes investigated in this study

Complex	S_0^2	First shell M–O			Second shell M–C			Third shell M–C			Multiple scattering M–C–O		
		N_O	R_O (Å)	σ_O^2 (Å^2)	N_{C2}	R_{C2} (Å)	σ_{C2}^2 (Å^2)	N_{C3}	R_{C3} (Å)	σ_{C3}^2 (Å^2)	N_{C-O}	R_{C-O} (Å^2)	σ_{C-O}^2 (Å^2)
Fe(III)Ent^{3-} (cat)[a]	0.87	6	2.00	0.0053	6	2.82	0.0052	ND	ND	ND	ND	ND	ND
Fe(III)H_3Ent (sal)[a]	0.86	6	1.98	0.0076	6	2.83	0.0049	ND	ND	ND	ND	ND	ND
Fe(III)Proto^{3-} (cat)	0.87[b]	5.3[5][d]	2.000[6]	0.0077[8]	6[e]	2.80[2]	0.010[2]	6[e]	4.32[3]	0.013[3]	12[e]	3.06[3]	0.005[4]
Fe(III)H_3Proto (sal)	0.87[b]	4.6[7][d]	1.97[1]	0.009[1]	6[e]	2.81[3]	0.015[3]	6[e]	4.26[5]	0.018[7]	12[e]	3.14[5]	0.03[1]
					3[e]	3.34[5]	0.012[7]						
Mn(III)Proto^{3-} (cat)	0.835[c]	4[e,f]	1.86[1]	0.0055[7]	6[e]	2.64[4]	0.010[3]	6[e]	4.16[4]	0.003[3]	12[e]	2.88[5]	0.006[5]
		2[e,f]	2.25[3]	0.009[4]									

Numbers in brackets represent uncertainty of the last decimal place of their respective values

[a] Data for Ent complexes is from Abergel et al. 2006

[b,c] Amplitude reduction factors were obtained from [b] (Duckworth et al. 2008a), and [c] (Webb et al. 2005a)

[d] ESD values are model-dependent standard deviations. If the atoms in this specific shell are non-normally distributed (as expected for Fe(III)H_3Proto and Fe(III)Proto^{3-} based on DFT, cf. Table S1), then the fit-derived N values may deviate significantly from physical reality, and this deviation may not be captured in the stated ESD

[e] Fixed coordination number

[f] $N = 4$ and $N = 2$ represent oxygen atoms located at axial ($N = 2$) and equatorial ($N = 4$) positions of a Jahn–Teller distorted complex

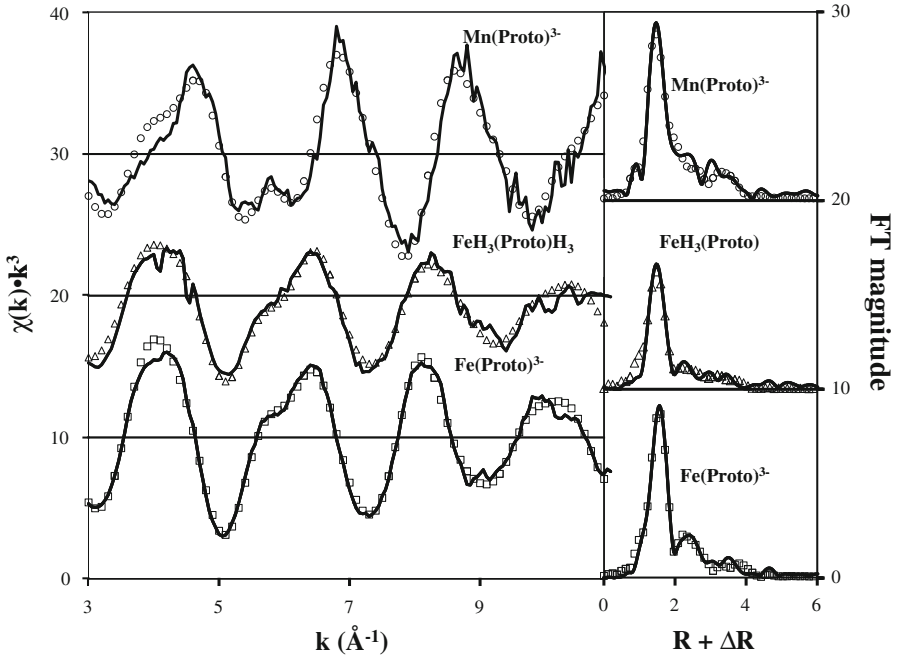

Fig. 8 K-edge EXAFS spectra of the Mn(III)Proto^{3-} complex, the Fe(III)Proto^{3-} complex bound through the catecholate binding mode, and the Fe(III)H_3Proto complex bound through the salicylate binding mode. *Solid lines* indicate experimental data, whereas *points* indicate the fit of a structural model. The optimized parameters used to produce the fit are shown in Table 2

center of the complex. This result demonstrates that the coordination environment of the Mn center is a distorted octahedron, arising from the Jahn–Teller effect, as previously noted for other Mn(III)–siderophore complexes (Duckworth et al. 2009a; Harrington et al. 2011b).

EXAFS measurements were also made of the protonated Fe(III)H_3Proto complex. As discussed above, at lower solution pH values, the catecholate groups are protonated, resulting in a shift in coordination modes to the salicylate binding mode. Upon protonation, the solubility of the complex decreases greatly due to the loss of its overall charge, and it precipitates out of solution as a neutral salt. As such, measurements of this complex were performed on a colloidal suspension of Fe(III)H_3Proto. The salicylate binding mode complex was determined using a similar three-shell model as the catecholate binding mode complex. The number of O atoms found in the inner coordination sphere, however, was found to be 4.6, slightly less than the expected six O atoms. The average distance of the oxygen atoms, was found to be 1.97 ± 0.01 Å, agreeing with a previous study of the salicylate binding mode of enterobactin with Fe(III) (R = 1.98 Å). Additionally, the second shell was fit at an average distance of 2.81 ± 0.03 Å, compared to 2.83 Å in the Fe(III)–enterobactin salicylate complex. These results demonstrate that the Fe–O bond lengths of the Fe(III)Proto^{3-} complex contract upon protonation. A similar observation was made in the Fe(III)-enterobactin system (Abergel et al. 2006). This contraction likely arises due to a combination of the coordination geometry of the salicylate binding mode (six-membered chelate ring) and the nature of the hybridization of the orbitals involved in coordination (one sp^2 and one sp^3 in salicylate binding mode and two sp^3 orbitals in catecholate binding mode).

The fits of complexes in catecholate coordination [viz. Mn(III)Proto^{3-} and Fe(III)Proto^{3-}] are improved by the inclusion of multiple scattering paths. Triangular multiple M–C–O paths were found to be at 2.88–3.14 Å, consistent with the geometry of the complex from SS paths and DFT-calculated structures (as discussed below). The paths were significant for Fe(III)Proto^{3-} and Mn(III)Proto^{3-} as indicated by improvement of the R-factor at the 95% confidence level (Hamilton 1965; Downward et al. 2006). For Fe(III)H_3Proto in salicylate coordination, inclusion of this shell does not improve the fit, but is included for self-consistency of the structural model (see Supplemental Material).

Comparison of the theoretical structures of the Fe(III)–protochelin complex with the structures determined by EXAFS reveals strong agreement between

the theoretical values and the experimentally-determined values (see Supplemental Material, Table S1). For the Fe(III) complexes, the Fe–O bond lengths that are calculated ($R = 2.04 \pm 0.06$ Å) are slightly longer than the values determined from the EXAFS analysis of the complex in solution (ca. 2.0 Å). The calculated Fe–O bond distances are not normally distributed (cf. Table S1), an insight which may help to explain low coordination numbers seen in structural fits of the Fe(III)–Proto complexes (Table 2). A non-normal distribution of atoms may result in a systematically low N as determined by EXAFS fitting, as is observed in the first shell of our fits for these complexes.

The simulation of Mn(III)Proto^{3-} is also consistent with structures determined from EXAFS fits. Calculated Mn–O distances agree well with the average 1st and 2nd shell distance fits. The distortion in this complex was predicted to take place in two M–O bonds that are situated trans- from each other, which is accommodated in the case of the rigid catecholate donor group by a change in the angle of coordination and a concurrent shortening of the second M–O bond length on the donor group. Although Jahn–Teller distortion normally occurs in a trans-configuration, which facilitates breaking the degeneracy of the e_g orbitals in an octahedral complex, it is interesting that a complex with rigid conjugated donor groups is flexible enough to allow such a structural transition to occur.

Relating complex structure to stability

Previous studies have shown that Mn(III)–siderophore complexes may have higher or lower stability constants than the corresponding Fe(III)-complexes (Duckworth et al. 2009a; Parker et al. 2004). A comparison of Mn(III)– and Fe(III)–siderophore complexes with DFOB and Proto (Table 1) suggests that catechol moieties have a larger preference for Fe(III) ($\Delta\log \beta_{110} = 3.0$) than hydroxamate groups ($\Delta\log \beta_{110} = 2.1$). It is possible that different siderophore moieties may favor the binding of specific metals. For example, catechol groups are particularly effective at binding Fe(III) (Albrecht-Gary and Crumbliss 1998), and may be slightly less effective at binding Mn(III). In contrast, carboxylate moieties may have a higher affinity for Mn(III) than Fe(III) (Ahrland et al. 1990). However, other structural factors may also affect the relative stability of complexes. Structural distortion of complexes away from ideal high-symmetry structures, as reflected in Debye–Waller factors and bond distances (Duckworth et al. 2009a), and by distortion of complex angles (Hay et al. 2001), have been shown to be strongly related to siderophore-metal complex stability. Mn(III) has a d^4 electronic configuration, which, as mentioned above with regard to trans O–M–O and O–C–C–O dihedral angles, results in a highly distorted octahedral coordination sphere due to the Jahn–Teller effect. Thus, both the binding moieties and overall architecture may help to determine the relative affinities of siderophores for Fe(III) and Mn(III). A more in-depth discussion of this concept will be provided in a future report (Harrington et al. 2011b).

Implications for metal transport and uptake

The results of the above experiments demonstrate that catecholate siderophores are able to form complexes with non-ferric metals Mn and Co, and that this chelation reaction can promote the air-oxidation of Mn(II) to Mn(III). However, the results also suggest that the Mn(III) complex that is formed is unstable at environmental conditions on a time frame of hours, and that the complex formed between Co(II) and protochelin degrades rapidly at any pH. These results have interesting implications for the role of catecholate siderophores in environmental cycling of metals. The chelation and subsequent air oxidation of Mn(II) results in the formation of a Mn(III)-complex with presumably lower stability than that of Fe(III) complexes. Although the stability constants differ by three orders of magnitude, this difference in stability may still be small enough to allow interference with iron uptake and metabolism by siderophores in environments that contain high concentrations of manganese, in a manner similar to what has been proposed for DFOB (Duckworth et al., 2009a).

The results of this study also have significant implications for the biological uptake of metals. In nature, some other catecholamide donor group siderophores have been observed to make use of hydrolysis reactions to assist in the intracellular release of complexed metals. The most notable example of this is enterobactin (Fig. 1), the Fe(III) complex of which is taken into the bacterial cell, where the trilactone ring is broken into three dihydroxybenzyl subunits to assist in the removal of Fe(III) (Abergel et al. 2009).

A similar hydrolysis reaction is also observed in the bacterial siderophore brasilibactin A, which also contains an ester group in its backbone. However, it is unclear whether this reaction plays any role in the physiological function of the siderophore (Harrington et al. 2011a). Although it is not possible to say with any certainty whether the degradation of protochelin is utilized to facilitate intracellular release of Fe(III), the possibility does exist due to the relative instability of the molecule.

The electrochemistry of protochelin suggests that the redox chemistry of the catecholate ligand may play a significant role in the release of metals after uptake. A redox reaction centered on the catechol donor groups could facilitate dissociation of the metal from the complex. A previous study investigated the electrochemistry of Mn–catechol complexes and showed that upon oxidation of the catechol groups as those in protochelin to quinone groups, their affinity for chelating metals is significantly reduced (Bodini et al. 1995), which may facilitate metal release. Ligand oxidation and metal release could be followed by reduction of the resulting quinone moieties back to catechol groups, regenerating the original siderophore. As mentioned above, some organisms make use of siderophore degradation to release Fe(III) from its complex. In the case of protochelin, however, it may be possible to release the metal from the siderophore through an electrochemical reaction without subsequent degradation of the ligand. This mechanism may allow the organism to avoid spending the metabolic cost associated with the production of a new molecule of the siderophore. We believe that the concept of ligand-redox facilitated metal release may be a novel idea in the field of biological metal uptake. Whereas the oxidation of the ligand was less able to take place in the experimental system upon chelation of a metal, in nature, small molecules could serve as the electron receivers, which may be better able to interact with the ligand than the surface of an electrode.

Protonation of the metal–ligand complex also can facilitate the removal of the metal from the complex. Although computational results predict Fe(III) to be the most difficult metal–protochelin complex to protonate, the complex undergoes a salicylate shift in coordination mode at circumneutral to acidic pH. This behavior has been proposed as having a role in the Fe(III) release mechanism of catecholamide siderophores; not only does the siderophore complex have lower affinity for binding 3+ metal ions in the salicylate binding mode, but there is also a drastic shift in the redox potentials of Fe(III) complexes, moving them into the range where Fe(III) can be reduced by biological reductants (Abergel et al. 2006; Rodgers et al. 1987).

The characteristics of metal selectivity that are suggested by this study as a result of ligand design may have broader implications for siderophore biogeochemistry. Another study is currently underway to systematically explore the role that donor group identity plays in metal selectivity of siderophores. The understanding that can be gained from such an analysis can provide a more thorough understanding of the roles of siderophores in trace metal cycling in the environment.

Acknowledgments We are grateful for support received from the National Science Foundation Geobiology and Low-Temperature Geochemistry Program (award number EAR-0921313). We thank Joe Rogers, Jasquelin Peña, Scott Calvin, and Martin Akafia for help during data collection at the synchrotron. We thank Dorothy Parker for valuable discussion. Portions of this research were carried out at the Stanford Synchrotron Radiation Lightsource, a Directorate of SLAC National Accelerator Laboratory and an Office of Science User Facility operated for the U.S. Department of Energy Office of Science by Stanford University. The SSRL Structural Molecular Biology Program is supported by the DOE Office of Biological and Environmental Research and by the National Institutes of Health, National Center for Research Resources, Biomedical Technology Program (P41RR001209), and the National Institute of General Medical Sciences. Mass spectra were obtained at the NCSU Department of Chemistry Mass Spectrometry Facility by Danielle Lehman. Funding for this facility was obtained from the North Carolina Biotechnology Center, and the NCSU Department of Chemistry.

References

Abergel RJ, Warner JA, Shuh DK, Raymond KN (2006) Enterobactin protonation and iron release: structural characterization of the salicylate coordination shift in ferric enterobactin. J Am Chem Soc J128:8920–8931

Abergel RJ, Zawadzka AM, Hoette TM, Raymond KN (2009) Enzymatic hydrolysis of trilactone siderophores: where chiral recognition occurs in enterobactin and bacillibactin iron transport. J Am Chem Soc 131(35):12682–12692

Ahrland S, Dahlgren A, Persson I (1990) Stabilities and hydrolysis of some iron(II) and manganese(III) complexes with chelating ligands. Acta Agric Scand 40:101–111

Albrecht-Gary AM, Crumbliss AL (1998) Coordination chemistry of siderophores: thermodynamics and kinetics of iron chelation and release. In: Sigel A, Sigel H (eds) Metal ions in biological systems. M. Dekker, New York

Bath BD, Michael DJ, Trafton BJ, Joseph JD, Runnels PL, Wightman RM (2000) Subsecond adsorption and desorption of dopamine at carbon-fiber microelectrodes. Anal Chem 72(24):5994–6002

Becke AD (1993) Density-functional thermochemistry. III. The role of exact exchange. J Chem Phys 98:5648–5652

Bellenger JP, Arnaud-Neu F, Asfari Z, Myneni SCB, Stiefel EI, Kraepiel AML (2007) Complexation of oxoanions and cationic metals by the biscatecholate siderophore azotochelin. J Biol Inorg Chem 12(3):367–376. doi:10.1007/s00775-006-0194-6

Bellenger JP, Wichard T, Kraepiel AML (2008a) Vanadium requirements and uptake kinetics in the dinitrogen-fixing bacterium *Azotobacter vinelandii*. Appl Environ Microbiol 74(5):1478–1484. doi:10.1128/aem.02236-07

Bellenger JP, Wichard T, Kustka AB, Kraepiel AML (2008b) Uptake of molybdenum and vanadium by a nitrogen-fixing soil bacterium using siderophores. Nat Geosci 1(4):243–246. doi:10.1038/Ngeo161

Bellenger JP, Wichard T, Xu Y, Kraepiel AML (2011) Essential metals for nitrogen fixation in a free-living N_2-fixing bacterium: chelation, homeostasis and high use efficiency. Environ Microbiol 13(6):1395–1411. doi:10.1111/j.1462-2920.2011.02440.x

Bodini M, Osorio C, Valle MAd, Aranciba V, Munoz G (1995) Redox chemistry of 3,4-dihydroxy-2-benzoic acid, its oxidation products and their interaction with manganese(II) and manganese(III). Polyhedron 14(20–21):2933–2936

Boukhalfa H, Reilly SD, Smith WH, Neu MP (2004) EDTA and mixed-ligand complexes of tetravalent and trivalent plutonium. Inorg Chem 43:5816

Boukhalfa H, Reilly SD, Neu MP (2007) Complexation of Pu(IV) with the natural siderophore desferrioxamine B and the redox properties of Pu(IV)(siderophore) complexes. Inorg Chem 46:1018

Buerge IJ, Hug SJ (1998) Influence of organic ligands on chromium(VI) reduction by iron(II). Environ Sci Technol 32:2092–2099

Carrano CJ, Drechsel H, Kaiser D, Jung G, Matzanke B, Winkelmann G, Rochel N, Albrecht-Gary AM (1996) Coordination chemistry of the carboxylate type siderophore rhizoferrin: the iron(III) complex and its metal analogs. Inorg Chem 35:6429–6436

Clarke ET, Tari LW, Vogel HJ (2001) Structural biology of bacterial iron uptake systems. Curr Top Med Chem 1:7

Cornish AS, Page WJ (1995) Production of the Triscatecholate Siderophore Protochelin by *Azotobacter vinelandii*. Biometals 8(4):332–338

Cornish AS, Page WJ (2000) Role of molybdate and other transition metals in the accumulation of protochelin by *Azotobacter vinelandii*. Appl Environ Microbiol 66(4):1580–1586

Crumbliss AL, Harrington JM (2009) Iron sequestration by small molecules: thermodynamic and kinetic studies of natural siderophores and synthetic model compounds. In: van Eldik R (ed) Advance in inorganic chemistry, vol 61. Elsevier, Amsterdam, pp 179–250

Dahlheimer SR, Neal CR, Fein JB (2007) Potential mobilization of platinum-group elements by siderophores in surface environments. Environ Sci Technol 41(3):870–875

Devlin HR, Harris IJ (1984) Mechanism of the oxidation of aqueous phenol with dissolved oxygen. Ind Eng Chem Fundam 23:387–392

Downward L, Booth CH, Lukens WW, Bridges FA (2006) Variation of the F-test for determining statistical relevance of particular parameters in EXAFS fits. In: Hedman B, Pianetta P (eds) 13th international conference on X-Ray absorption fine structure. Stanford Synchrotron Radiation Laboratory, Stanford

Duckworth OW, Sposito G (2005) Siderophore–manganese(III) interactions I. Air-oxidation of manganese(II) promoted by desferrioxamine B. Environ Sci Technol 39:6037–6044

Duckworth OW, Bargar JR, Sposito G (2008) Sorption of ferric iron from ferrioxamine B to synthetic and biogenic layer type manganese oxides. Geochim Cosmochim Acta 72:3371–3380

Duckworth OW, Bargar JR, Sposito G (2009a) Quantitative structure–activity relationships for aqueous metal–siderophore complexes. Environ Sci Technol 43:343–349

Duckworth OW, Holmström SJM, Pena J, Sposito G (2009b) Biogeochemistry of iron oxidation in a circumneutral freshwater habitat. Chem Geol 260(3–4):149–158

Duckworth OW, Jarzecki AA, Bargar JR, Oyerinde O, Spiro TG, Sposito G (2009c) An exceptionally stable cobalt(III)–desferrioxamine B complex. Mar Chem 113:114–122

Duhme AK, Hider RC, Khodr HH (1997) Synthesis and iron-binding properties of protochelin, the tris(catecholamide) siderophore of Azotobacter vinelandii. Chem Ber Recueil 130:969–973

Duhme AK, Hider RC, Naldrett MJ, Pau RN (1998) The stability of the molybdenum–azotochelin complex and its effect on siderophore production in *Azotobacter vinelandii*. J Biol Inorg Chem 3(5):520–526

Essén SA, Bylund D, Holmström SJA (2006) Quantification of hydroxamate siderophores in soil solutions of podzolic soil profiles in Sweden. Biometals 19(3):269–282

Frazier SW, Kretzschmar K, Kraemer SM (2005) Bacterial siderophores promote dissolution of UO2 under reducing conditions. Environ Sci Technol 39(15):5709–5715

Frisch MJ, Trucks GW, Schlegel HB, Scuseria GE, Robb MA, Cheeseman JR, Scalmani G, Barone V, Mennucci B, Petersson GA, Nakatsuji H, Caricato M, Li X, Hratchian HP, Izmaylov AF, Bloino J, Zheng G, Sonnenberg JL, Hada M, Ehara M, Toyota K, Fukuda R, Hasegawa J, Ishida M, Nakajima T, Honda Y, Kitao O, Nakai H, Vreven T, Montgomery J, A J, Peralta JE, Ogliaro F, Bearpark M, Heyd JJ, Brothers E, Kudin KN, Staroverov VN, Kobayashi R, Normand J, Raghavachari K, Rendell A, Burant JC, Iyengar SS, Tomasi J, Cossi M, Rega N, Millam NJ, Klene M, Knox JE, Cross JB, Bakken V, Adamo C, Jaramillo J, Gomperts R, Stratmann RE, Yazyev O, Austin AJ, Cammi R, Pomelli C, Ochterski JW, Martin RL, Morokuma K, Zakrzewski VG, Voth GA, Salvador P, Dannenberg JJ, Daniels S, Dapprich AD, Farkas Ö, Foresman JB, Ortiz JV, Cioslowski J, Fox DJ (2009) Gaussian 09. B, 1st edn. Gaussian Inc., Wallingford

Gans P, Sabatini A, Vacca A (1996) Investigation of equilibria in solution. Determination of equilibrium constants with HYPERQUAD suite of programs. Talanta 43(10):1739–1753

Hamilton WC (1965) Significance tests on the crystallographic R factor. Acta Crystallogr 18:502–510

Harrington JM, Park H, Ying Y, Hong J, Crumbliss AL (2011a) Characterization of Fe(III) sequestration by an analog of the cytotoxic siderophore brasilibactin A: implications for the iron transport mechanism in mycobacteria. Metallomics 3:464–471

Harrington JM, Parker DL, Jarzecki AA, Bargar JR, Tebo BM, Duckworth OW (2011b) Structural dependence of manganese chelation by siderophores: Donor group dependence of complex stability and reactivity. Geochim Cosmochim Acta (inpress)

Harris WR, Carrano CJ, Raymond KN (1979a) Coordination chemistry of microbial iron transport compounds. 16. Isolation, characterization, and formation constants of ferric aerobactin. J Am Chem Soc 101:2722

Harris WR, Carrano CR, Cooper SR, Sofen SR, Avdeef AE, McArdle JV, Raymond KN (1979b) Coordination chemistry of microbial iron transport compounds. 19. Stability constants and electrochemical behavior of ferric enterobactin and model complexes. J Am Chem Soc 101:6097–6104

Harris WR, Amin SA, Kuepper FC, Green DH, Carrano CJ (2007) Borate binding to siderophores: structure and stability. J Am Chem Soc 129:12263

Hay BP, Dixon DA, Vargas R, Garza J, Raymond KN (2001) Structural criteria for the rational design of selective ligands. 3. Quantitative structure–stability relationship for Iron(III) complexation by tris-catecholamide siderophores. Inorg Chem 40:3922–3935

Heien M, Johnson MA, Wightman RM (2004) Resolving neurotransmitters detected by fast-scan cyclic voltammetry. Anal Chem 76(19):5697–5704. doi:10.1021/ac0491509

Hernlem BJ, Vane LM, Sayles GD (1999) The application of siderophores for metal recovery and waste remediation: examination of correlations for prediction of metal affinities. Water Resour 33:951–960

Hewkin DJ, Prince RH (1970) The mechanism of octahedral complex formation by labile metal ions. Coord Chem Rev 5:45–73

Hider RC, Kong X (2010) Chemistry and biology of siderophores. Nat Prod Rep 27:637–657

Holmström SJA, Lundstrom US, Finlay RD, Van Hees PAW (2004) Siderophores in forest soil solution. Biogeochemistry 71(2):247–258

Hou Z, Stack TDP, Sunderland CJ, Raymond KN (1997) Enhanced iron(III) chelation through ligand predisposition: syntheses, structures and stability of tris-catecholate enterobactin analogs. Inorg Chim Acta 263:341–355

Kelly SD, Hesterberg D, Ravel B (2008) Analysis of soils and minerals using X-ray absorption spectroscopy. In: Ulery AL, Drees LR (eds) Methods of soil analysis. Soil Science Society of America, Madison

Khodr HH, Hider RC, Duhme-Klair AK (2002) The iron-binding properties of aminochelin, the mono(catecholamide) siderophore of *Azotobacter vinelandii*. J Biol Inorg Chem 7(7–8):891–896. doi:10.1007/s00775-002-0375-x

Kohler T, Armbruster T, Libowitzky E (1997) Hydrogen bonding and Jahn–Teller distortion in groutite, α-MnOOH, and manganite, γ-MnOOH, and their relations to the manganese dioxides ramsdellite and pyrolusite. J Solid State Chem 133:486–500

Kraemer SM (2004) Iron oxide dissolution and solubility in the presence of siderophores. Aquat Sci 66:3–18

Kraemer SM, Butler A, Borer P, Cervini-Silva J (2005) Siderophores and the dissolution of iron-bearing minerals in marine systems. In: Banfield JF, Cervini-Silva J, Nealson KH (eds) Molecular geomicrobiology, vol 5. Mineralogical Society of America, Chantilly

Kraepiel AML, Bellenger JP, Wichard T, Morel FMM (2009) Multiple roles of siderophores in free-living nitrogen-fixing bacteria. Biometals 22(4):573–581. doi:10.1007/s10534-009-9222-7

Lee C, Yang W, Parr RG (1988) Development of the Colle–Salvetti correlation-energy formula into a functional of the electron density. Phys Rev B 37:785–789

Levina A, Armstrong RS, Lay PA (2005) Three-dimensional structure determination using multiple-scattering analysis of XAFS: applications to metalloproteins and coordination chemistry. Coord Chem Rev 249:141–160

Loomis LD, Raymond KN (1991) Solution equilibria of enterobactin and metal–enterobactin complexes. Inorg Chem 30:906–911

Marschner H, Romheld V, Kissel M (1986) Different strategies in higher plants inmobilization and uptake of iron. J Plant Nutr 9:695–713

Martell AE, Smith RM (2003) Critical stability constant database. National Institute of Science and Technology (NIST), Gaithersburg

Mawji E, Gledhill M, Milton JA, Tarran GA, Ussher S, Thompson A, Wolff GA, Worsfold PJ, Achterbeg EP (2008) Hydroxamate siderophores: occurrence and importance in the Atlantic Ocean. Environ Sci Technol 42(23):8675–8680

Mishra B, Haack EA, Maurice PA, Bunker BA (2009) Effects of the microbial siderophore DFO-B on Pb and Cd speciation in aqueous solution. Environ Sci Technol 43(1):94–100

Mucha P, Rekowski P, Kosakowska A, Kupryszewski G (1999) Separation of siderophores by capillary electrophoresis. J Chromatogr A 830(1):183–189

Neu MP, Icopini GA, Boukhalfa H (2005) Plutonium speciation affected by environmental bacteria. Radiochim Acta 93:705

Newville M (2001) *IFEFFIT*: interactive XAFS analysis and *FEFF* fitting. J Synchrotron Rad 8:322–324

Parker DL, Sposito G, Tebo BM (2004) Manganese(III) binding to a pyoverdine siderophore produced by a manganese(II)-oxidizing bacterium. Geochim Cosmochim Acta 68:4809–4820

Parker DL, Morita T, Mozafarzadeh ML, Verity R, McCarthy JK, Tebo BM (2007) Inter-relationships of MnO_2 precipitation, siderophore–Mn(III) complex formation, siderophore degradation, and iron limitation in Mn(III)-oxidizing bacterial cultures. Geochim Cosmochim Acta 71:5672

Raymond KN, Dertz EA (2004) Biochemical and physical properties of siderophores. In: Crosa JH, Rey AR, Payne SM (eds) Iron transport in bacteria. ASM, Washington, p 3

Rehr JJ, Kas JJ, Prange MP, Sorini AP, Takimoto Y, Vila F (2009) Ab initio theory and calculations of X-ray spectra. C R Phys 10(6):548–559

Renshaw JC, Robson GD, Trinci APJ, Wiebe MG, Livens FR, Collison D, Taylor RJ (2002) Fungal siderophores: structures, functions and applications. Mycol Res 106:1123

Roberts JG, Moody BP, McCarty GS, Sombers LA (2010) Specific oxygen-containing functional groups on the

carbon surface underlie an enhanced sensitivity to dopamine at electrochemically pretreated carbon fiber microelectrodes. Langmuir 26(11):9116–9122. doi:10.1021/la9048924

Rodgers SJ, Lee CW, Ng CY, Raymond KN (1987) Ferric ion sequestering agents. 15. Synthesis, solution chemistry, and electrochemistry of a new cationic analogue of enterobactin. Inorg Chem 26:1622–1625

Sanford AL, Morton SW, Whitehouse KL, Oara HM, Lugo-Morales LZ, Roberts JG, Sombers LA (2010) Voltammetric detection of hydrogen peroxide at carbon fiber microelectrodes. Anal Chem 82:5205–5210

Schwarzenbach G, Schwarzenbach K (1963) Hydroxamatkomplexe I. Die Stabilität der Eisen(III)-Komplexe einfacher Hydroxamsäuren und des Ferrioxamins B. Helv Chim Acta 46:1390–1400

Schweigert N, Zehnder AJB, Eggen RIL (2001) Chemical properties of catechols and their molecular modes of toxic action in cells, from microorganisms to mammals. Environ Microbiol 3(2):81–91

Selig H, Keinath TM, Weber WJ (2003) Sorption and manganese-induced oxidative coupling of hydroxylated aromatic compounds by natural geosorbents. Environ Sci Technol 37:4122–4127

Shannon RD (1976) Revised effective ionic radii and systematic studies of interatomic distances in halides and chalcogenides. Acta Crystallogr A32:751–767

Strathmann TJ, Stone AT (2002) Reduction of the pesticides oxamyl and methomyl by Fe(II): effect of pH and inorganic ligands. Environ Sci Technol 36:653–661

Szabo O, Farkas E (2011) Characterization of Mn(II) and Mn(III) binding capability of natural siderophores desferrioxamine B and desferricoprogen as well as model hydroxamic acids. Inorg Chim Acta 376:500–508

Taraz K, Ehlert G, Geisen K, Budzikiewicz H, Korth H, Pulverer Z (1990) Chemicals from bacteria. 40. Protocheline-A catecholate siderophore from a bacterium (DMS no. 5746). Z Naturforsch 45b:1327–1332

Tebo BM, Johnson HA, McCarthy JK, Templeton AS (2005) Geomicrobiology of manganese(II) oxidation. Trends Microbiol 13(9):421–428

Tomasi J, Mennucci B, Cammi R (2005) Quantum mechanical continuum solvation models. Chem Rev 105:2999–3094

Webb SM (2005) SIXPACK: a graphical user interface for XAS analysis using IFEFFIT. Phys Scr T115:1011–1014

Webb SM, Dick GJ, Bargar JR, Tebo BM (2005a) Evidence for the presence of Mn(III) intermediates in the bacterial oxidation of Mn(II). Proc Natl Acad Sci USA 102(15):5558–5563

Webb SM, Tebo BM, Bargar JR (2005b) Structural characterization of biogenic Mn oxides produced in seawater by the marine *bacillus* sp. strain SG-1. Am Min 90(8–9):1342–1357

Wichard T, Bellenger JP, Loison A, Kraepiel AML (2008) Catechol siderophores control tungsten uptake and toxicity in the nitrogen-fixing bacterium *Azotobacter vinelandii*. Environ Sci Technol 42(7):2408–2413. doi:10.1021/Es702651f

Winkelmann G (2004) Ecology of Siderophores. In: Crosa JH, Rey AR, Payne SM (eds) Iron transport in bacteria. ASM, Washington, p 437

Winkelmann G (2007) Ecology of siderophores with special reference to the fungi. Biometals 20:379–392